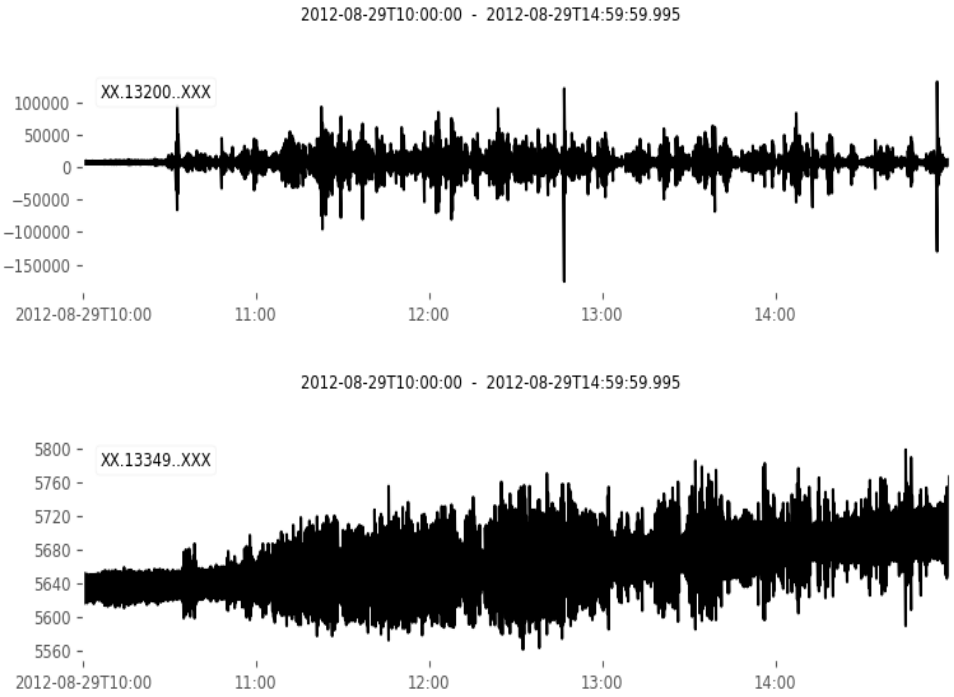
Supplementary Materials: Application of Seismic Noise Interferometry to Extract High-Resolution P-Wave Reflectivity and Near-Surface Velocity Structure from Hydraulic Fracturing Data

Joan Manuel Flores López [1] and Aderson Farias do Nascimento [1,2]*

Supplementary Figures

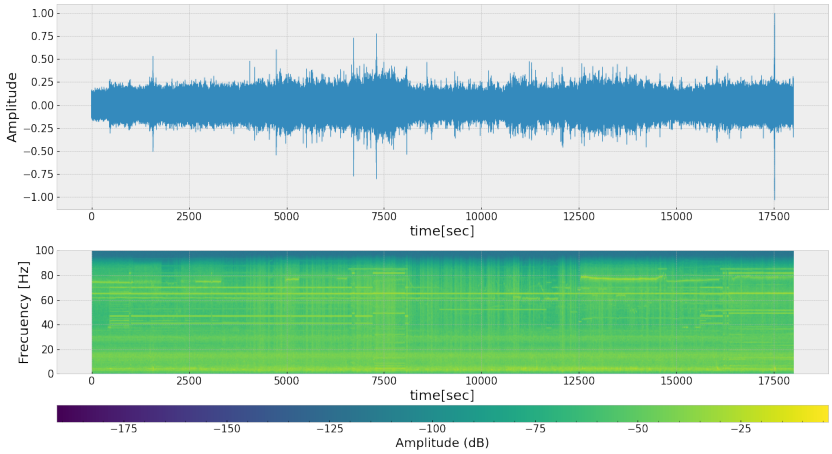
This section contains supplementary figures that provide additional technical details, intermediate processing results, and supporting data for the main manuscript. These figures are organized by topic and include raw data, processing parameters, and validation results.

S1. Raw data

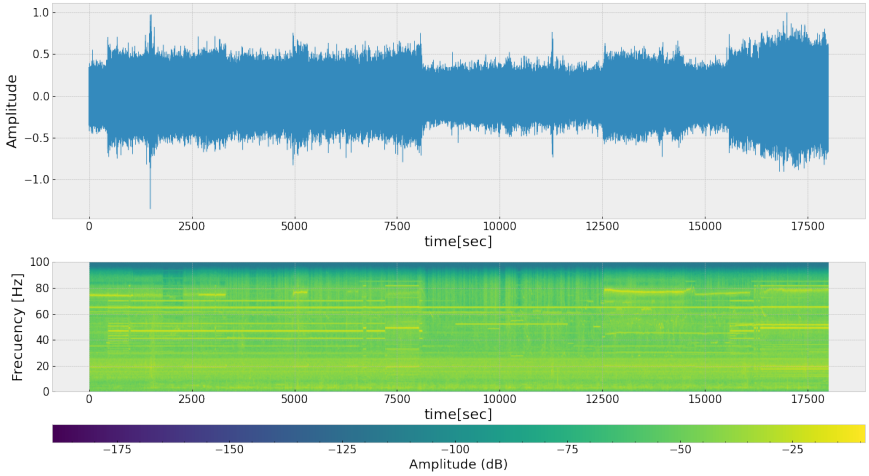


S1: Raw noise data recorded during the hydraulic fracturing monitoring experiment in the Potiguar Basin we used in our work. The time series show continuous ambient noise and induced seismic signals from the hydraulic fracturing process.

S2. Frequency analysis



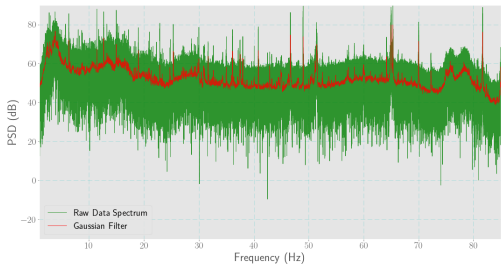
(**a**) First station, Line 04



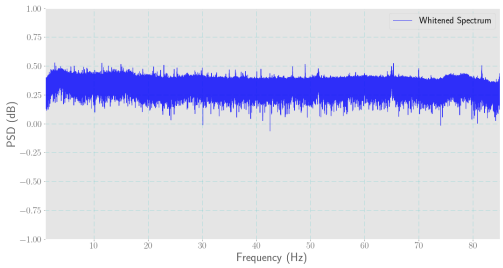
(**b**) First station, Line 02

S2: Amplitude and frequency spectrum of the first station for Lines 02 and 04. Figure (a) displays a relative increase in amplitude near 17,000 seconds, which corresponds to the start of hydraulic fracturing. A resonance peak is observed at frequencies of 40 and 80 Hz during this time interval. Figure (b) shows that the same event was not recorded with the same amplitude characteristics in Line 02.

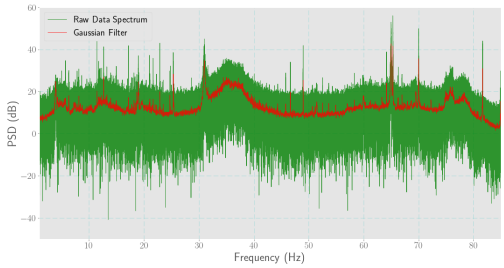
S3. Processing details: Gaussian smoothing and spectral whitening



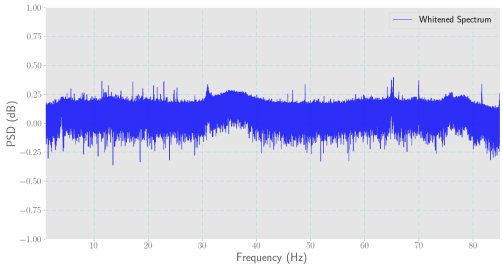
(**a**) Data spectrum, Line 01



(**b**) Whitened spectrum, Line 01



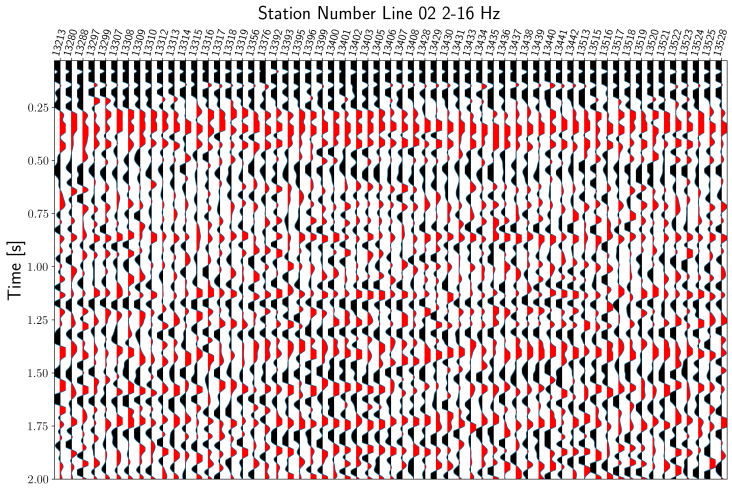
(**c**) Data spectrum, Line 03



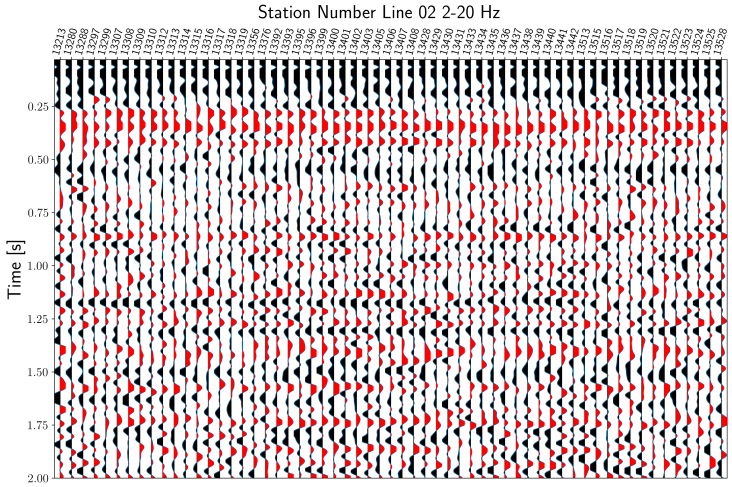
(**d**) Whitened spectrum, Line 03

S3: Gaussian smoothing filtering process and spectral whitening. Figures (a) and (c) show the raw data spectrum with the applied Gaussian smoothing filter (red curve overlay) for the first stations of Lines 01 and 03, respectively. Figures (b) and (d) show the corresponding whitened spectra obtained by dividing the raw spectrum by the smoothed spectrum. This whitening process removes the effects of microseismic peaks and enhances the frequency content for autocorrelation analysis.

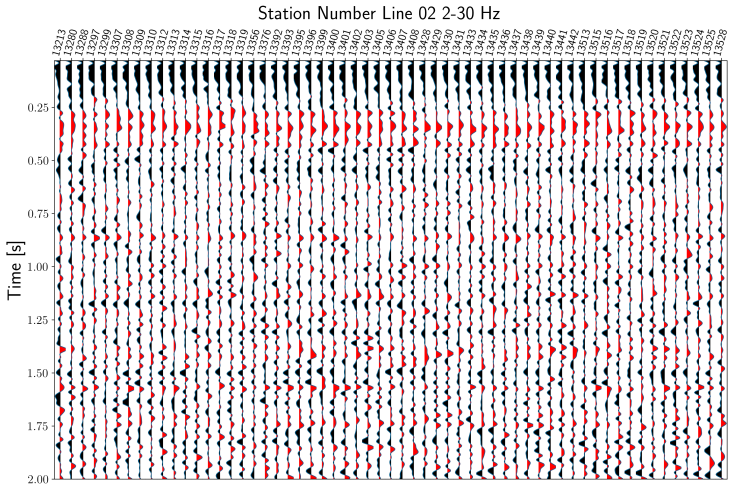
S4. Autocorrelation window analysis



(**a**) Frequency range 2–16 Hz



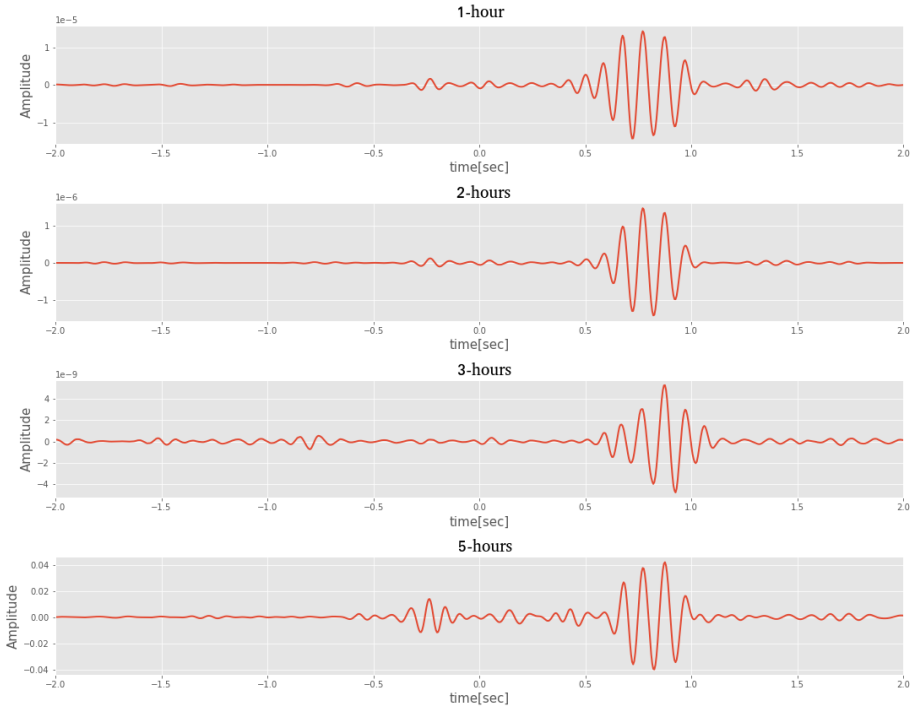
(**b**) Frequency range 2–20 Hz



(**c**) Frequency range 2–30 Hz

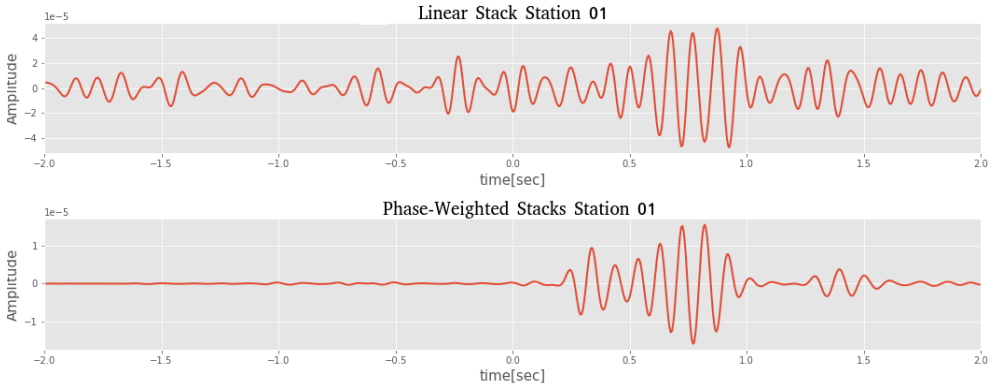
S4: Autocorrelation wiggles for Line 02 showing the calculation of autocorrelations for each recording station. The wiggle traces display the continuity of amplitudes at different depths and the effect of different frequency band-pass filters. Each panel shows the autocorrelation results for a specific frequency range: (a) 2–16 Hz, (b) 2–20 Hz, and (c) 2–30 Hz. These results demonstrate how the window length (15 seconds) and frequency filtering affect the definition of reflectors in the final seismic image.

S5. Cross-correlation window length analysis

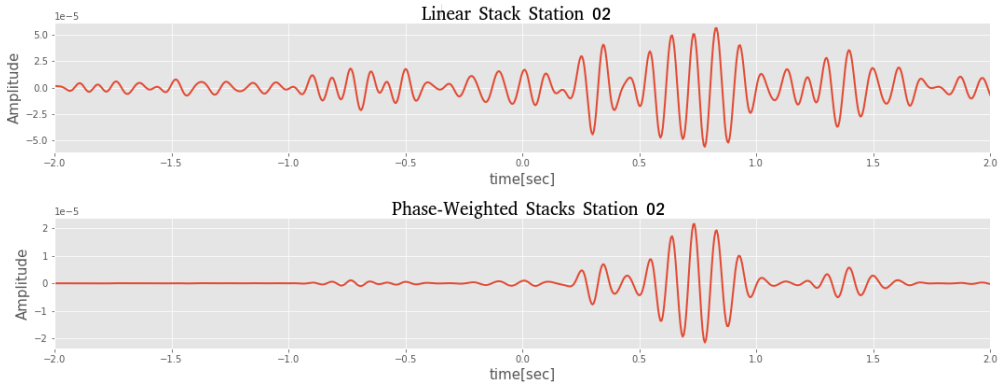


S5: Comparison of cross-correlation results using different data window lengths: 1, 2, 3, and 5 hours of continuous data, respectively. The results demonstrate that a 1-hour window is sufficient to robustly extract surface waves for S-wave velocity estimation. Increasing the data length beyond 1 hour does not significantly improve the quality of the surface-wave extraction, indicating that the signal-to-noise ratio is adequate with this window length.

S6. Stacking method comparison



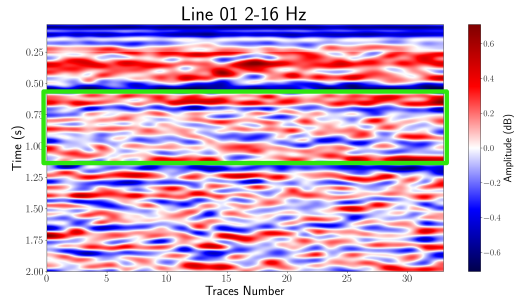
(**a**) First station, Line 04



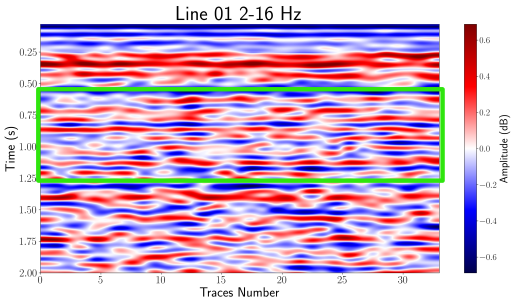
(**b**) First station, Line 02

S6: Comparison between linear stacking and Phase-Weighted Stacking (PWS) methods. Each panel shows the comparison for a specific station. The Phase-Weighted Stacking approach enhances coherent signals while suppressing incoherent noise, thereby improving the signal-to-noise ratio compared to conventional linear stacking. This method was selected as the optimal processing approach for the cross-correlation analysis in this study.

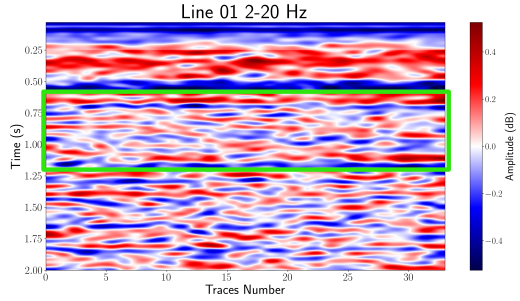
S7. Ambient noise vs. induced fracturing comparison



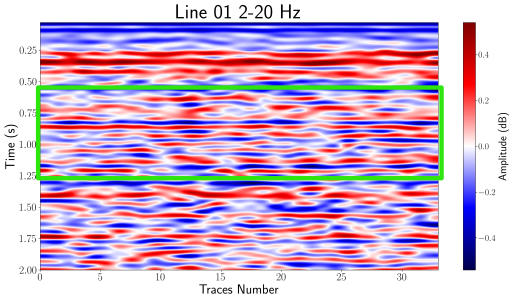
(**a**) Fracturing, 2–16 Hz



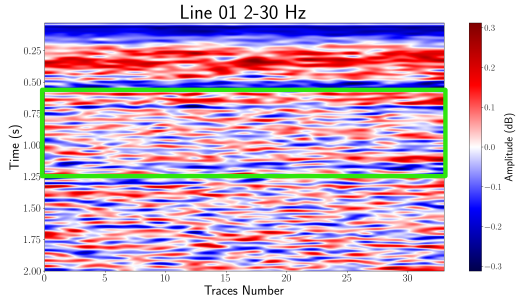
(**b**) Ambient noise, 2–16 Hz



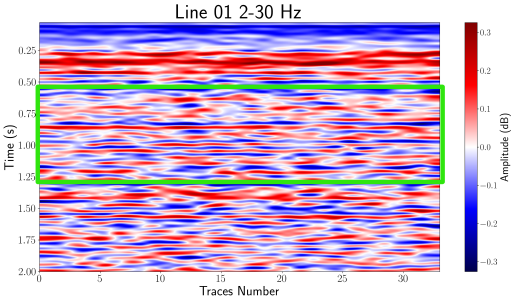
(**c**) Fracturing, 2–20 Hz



(**d**) Ambient noise, 2–20 Hz



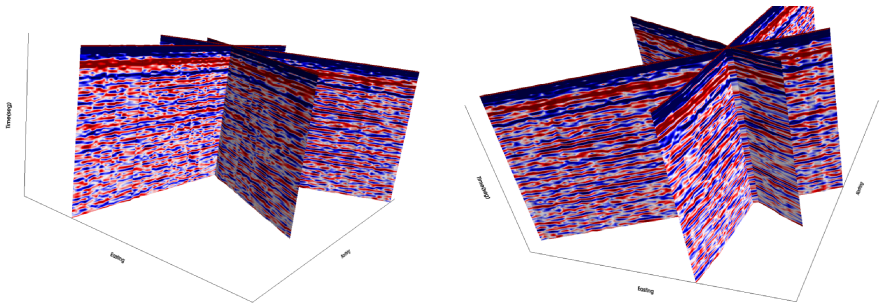
(**e**) Fracturing, 2–30 Hz



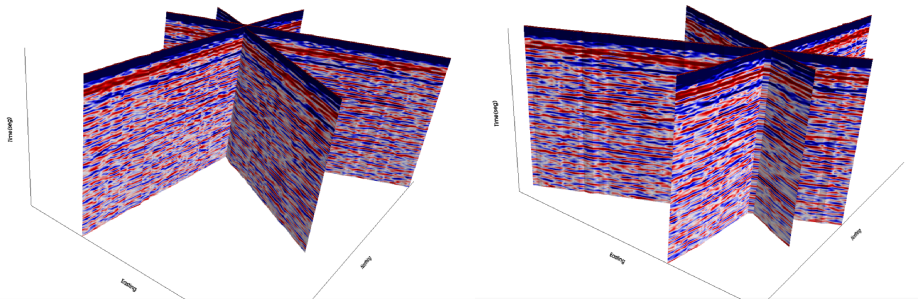
(**f**) Ambient noise, 2–30 Hz

S7: Comparison of autocorrelation results for Line 01 between ambient noise and induced fracturing periods. Left panels show results during the hydraulic fracturing interval, while right panels show results during ambient noise conditions. Three frequency ranges are compared: (a-b) 2–16 Hz, (c-d) 2–20 Hz, and (e-f) 2–30 Hz. The seismic sections obtained during fracturing show significantly better reflector definition and consistency, particularly at higher frequencies, demonstrating the effectiveness of using induced seismic signals as a noise source for high-resolution imaging.

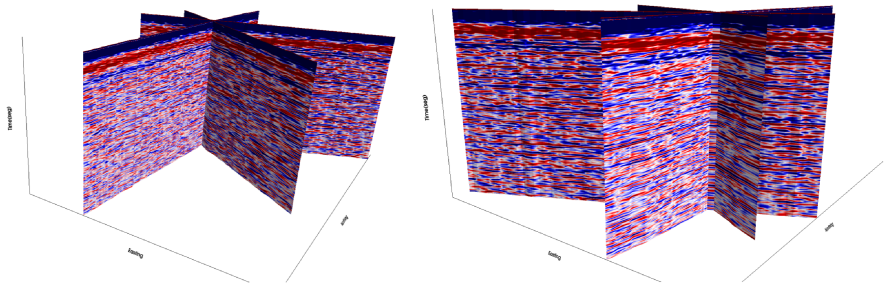
S8. Three-dimensional visualization



(**a**) Frequency range 2–16 Hz



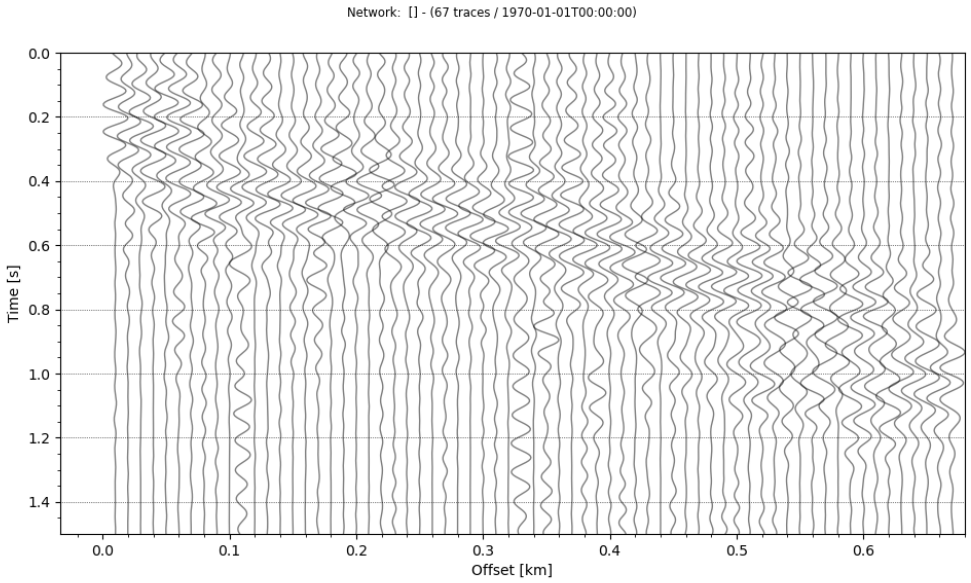
(**b**) Frequency range 2–20 Hz



(**c**) Frequency range 2–30 Hz

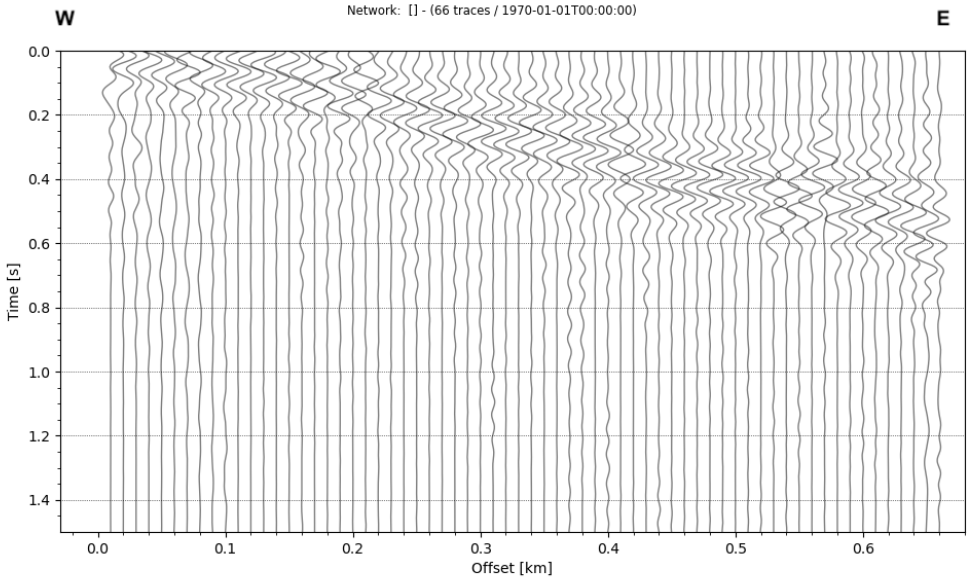
S8: Three-dimensional visualization of the seismic results showing the consistency and continuity of reflectors across the three survey lines. Each panel displays the 3D view for a specific frequency cutoff: (a) 2–16 Hz, (b) 2–20 Hz, and (c) 2–30 Hz. The 3D representation demonstrates that the main reflectors maintain their lateral continuity at the intersections of the three seismic sections, thereby validating the reliability of the autocorrelation-based imaging approach across different frequency bands.

S9. Surface wave extraction: Line 04 (virtual source) and Line 03 (receivers)



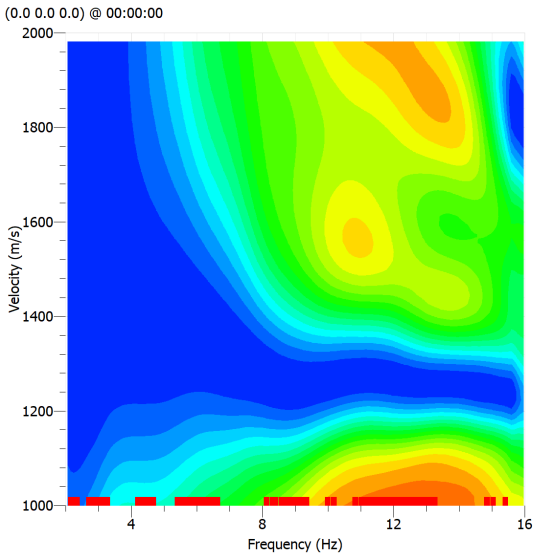
S9: Extracted surface waves from cross-correlation between Line 04 (virtual source) and Line 03 (receivers). This configuration uses the largest available offset (1450 m) to extract surface waves with the longest possible wavelength, enabling greater penetration depth. The frequency range used is 2–16 Hz. The seismogram shows the wave-train arrival and propagation characteristics used for dispersion-curve calculation and S-wave velocity inversion.

S10. Surface wave extraction within Line 03 only

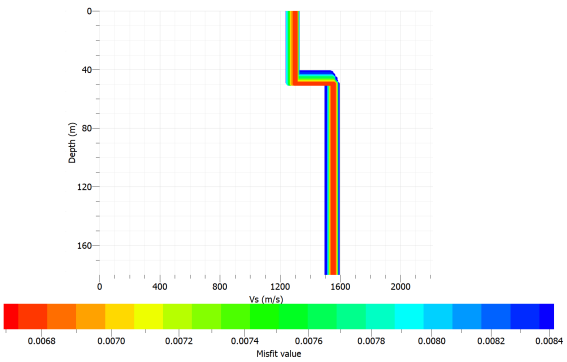


S10: Extracted surface waves from cross-correlation within Line 03 only (virtual source at the easternmost station near the well, receivers along the line). This configuration uses shorter offsets (10–660 m) and provides a higher signal-to-noise ratio than the longer-offset configuration. The frequency range is 2–16 Hz. This dataset is used to determine the S-wave velocity model for the shallow subsurface.

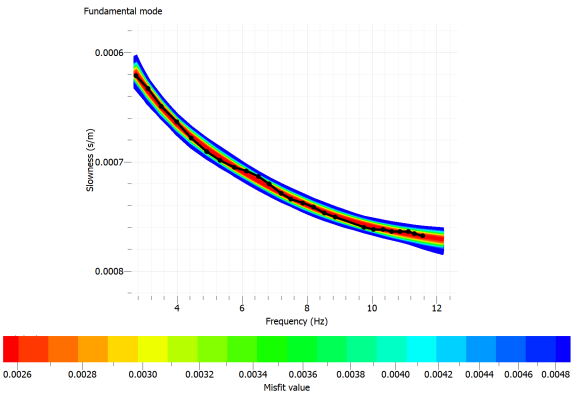
S11. Dispersion curves inversion-Cross01



(**a**) Dispersion curve



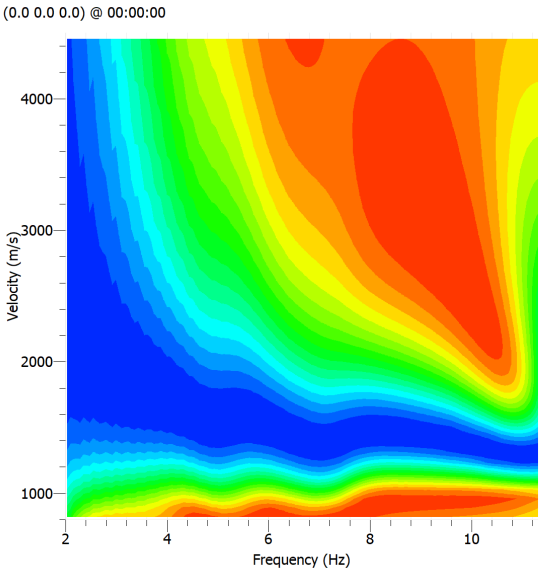
(**b**) S-wave velocity model



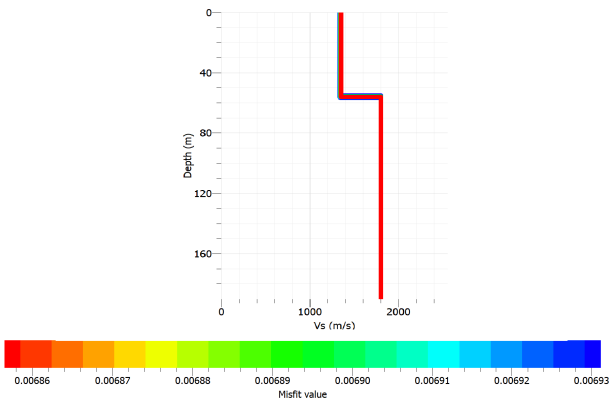
(**c**) Misfit error

S11: Dispersion curve and velocity model obtained from cross-correlation calculations between Line 04 and Line 03 (Cross01 configuration). Panel (a) shows the experimental dispersion curve extracted from the surface wave data. Panel (b) displays the resulting S-wave velocity model obtained through inversion using the Dinver algorithm. Panel (c) shows the misfit error between the observed and modeled dispersion curves. The S-wave velocity is approximately 1350 m/s, consistent with ground roll velocities commonly reported in the area. The weathered layer thickness is approximately 50 m, with an estimated maximum penetration of 180m.

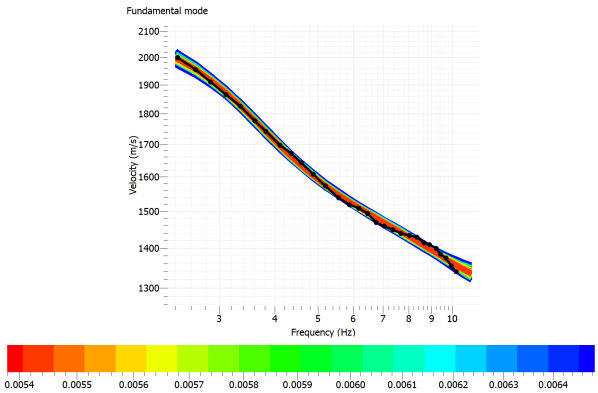
S12. Dispersion curves inversion-Cross02



(**a**) Dispersion curve



(**b**) S-wave velocity model



(**c**) Misfit error

S12: Dispersion curve and velocity model obtained from cross-correlation calculations within Line 03 only (Cross02 configuration). Panel (a) shows the experimental dispersion curve with a better signal-to-noise ratio due to shorter offsets. Panel (b) displays the resulting S-wave velocity model. Panel (c) shows the misfit e rror. This configuration provides complementary information about the shallow velocity structure and validates the results from the longer-offset configuration. The consistent S-wave velocity values between both configurations (approximately 1350 m/s) support the reliability of the velocity estimates.